Heliyon 9 (2023) e22635

Contents lists available at ScienceDirect

Heliyon

journal homepage: www.cell.com/heliyon

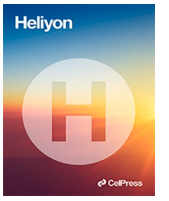

Photocatalytic NO_x removal with TiO_2-impregnated 3D-printed PET supports

G.F. Binetti Basterrechea [a], V.N. Montesinos [a,b,*], N. Quici [a,b,**]

[a] Centro Tecnologías Químicas – Dpto. de Ingeniería Química, FRBA, UTN, Medrano 951, Ciudad Autónoma de Buenos Aires, Argentina
[b] Gerencia de Química – CNEA, CONICET, Av. Gral. Paz 1499, Villa Maipú, Argentina

A B S T R A C T

In this work, we investigated the photocatalytic removal of NO_x using 3D-printed supports. Monolithic supports with internal channels were fabricated by Fused Modelling Deposition (FDM) using PET as the filament feedstock. The printing parameters of the supports were optimized to maximize the exposure of the photocatalyst to UV light throughout the monolithic PET printed supports. The removal experiments were carried out in a continuous gas phase flow reactor, which was custom designed in-house incorporating a 3D printed PET support impregnated with TiO_2 as photocatalyst. The impregnated and non-impregnated supports were characterized by diffuse reflectance spectrometry, SEM and AFM. The effect of several key-factors on the NO_x removal capacity was investigated, including the type of PET filament (native recycled, BPET vs. glycol-modified, PETG), the type of TiO_2 (P25 vs. Hombikat UV-100), the UV light source (LED vs. tubular lamps), and the number of deposited TiO_2 layers. The highest NO and NO_x removal were achieved by using PETG supports coated with a single layer of Hombikat UV-100 and irradiating the flat reactor from both sides using two sets of black light lamps. However, the highest selectivity toward nitrate formation was obtained when using P25 under the same experimental conditions. This work demonstrates that 3D printing is a reliable and powerful technique for fabricating photocatalytic reactive supports that can serve as a versatile platform for evaluating photocatalytic performance.

1. Introduction

In the past decade, 3D printing technology has successfully integrated into chemical engineering and catalytic technology [1]. By sidestepping intricate manufacturing processes, 3D printing revolutionizes the pathway from raw materials to functional devices, encompassing design and operation. Utilizing 3D printing facilitates the production of a wide range of supports, offering limitless variations in attributes like size, shape, mechanical strength, light transmittance, number of channels, and other important properties [2].

In reactor design applications, the versatility and convenience of using 3D-printed reactors have been demonstrated for organic compound synthesis through flow techniques, online monitoring, for the development of devices for chemical synthesis and purification [3–6], the fabrication of bubble microbioreactor [7] and numerous other domains, including catalytic applications [8]. Also, 3D printing has gained significant attraction in diverse photocatalytic applications. Li et al. ([9] and references therein) have presented a comprehensive review highlighting the advancements in the utilization of 3D printing for crafting substrates and catalysts in photocatalytic applications. When using a photocatalyst, the imperative of immobilization arises, particularly, in gas phase applications. In such instances, the immobilization of photocatalysts onto substrates becomes a necessity, with material transmittance and substrate

* Corresponding author. Centro Tecnologías Químicas – Dpto. de Ingeniería Química, FRBA, UTN, Medrano 951, Ciudad Autónoma de Buenos Aires, Argentina.

** Corresponding author. Centro Tecnologías Químicas – Dpto. de Ingeniería Química, FRBA, UTN, Medrano 951, Ciudad Autónoma de Buenos Aires, Argentina.

E-mail address: vnmontesinos@frba.utn.edu.ar (V.N. Montesinos).

https://doi.org/10.1016/j.heliyon.2023.e22635
Received 19 October 2023; Received in revised form 15 November 2023; Accepted 15 November 2023
Available online 21 November 2023

geometry emerging as pivotal factors for system optimization. Consequently, the design and production of monoliths as substrates offers a compelling alternative. In contrast to conventional fixed-bed reactors, monoliths boast advantages as an augmented external catalyst surface area, lower pressure drop, mitigation of obstructions, ease of handling for cleaning and maintenance, and prevention of the particulate scattering and material loss, between others benefits [10].

Monoliths produced through 3D technology have found utility across diverse domains, encompassing gas adsorption and separation processes [11–13] including their photocatalytic application [14]. The primary methodologies employed in 3D printing for photocatalytic applications involve extrusion-based printing [15], stereolithography [16], and powder-based printing.

Fused Deposition Modelling (FDM) offers a practical solution for photocatalytic applications, without the need for expensive equipment. This extrusion-based 3D printing technology can be seamlessly executed using a standard desktop FDM printer. The straightforward fabrication process, characterized by its cost-effectiveness and time efficiency, paves the way for reimagining and revamping reactor designs within laboratory contexts. In the realm of environmental applications for photocatalysis, a pivotal research goal lies in the optimization of reactor design to enhance the inherently slow reaction kinetics and scale-up the process [2].

This study underscores the advantages associated with the incorporation of 3D printing technology, complemented by cost-effective filament and an economical 3D printer, for the rapid fabrication of TiO_2-immobilized monoliths. To exemplify this approach, we utilize the nitrogen oxides removal reaction as a test case. Nitrogen oxides (NO_x), comprising nitric oxide (NO) and nitrogen dioxide (NO_2), are among the most toxic gases produced by various human activities [17]. Photocatalytic oxidation of NO_x has arisen as a viable strategy for eliminating NO_x through three consecutive one-electron transfer steps with HONO and NO_2 as intermediates by direct reaction with h^+_{VB} or mediated by reactive oxygen species (ROS) such as superoxide ($O_2^{\bullet-}$), hydrogen peroxide (H_2O_2) or hydroxyl radicals ($HO^\bullet$) (equation [1]):

$$NO^\bullet \xrightarrow{ROS,fast} HONO \xrightarrow{ROS,slow} NO_2 \xrightarrow{ROS,fast} HNO_3 \quad [1]$$

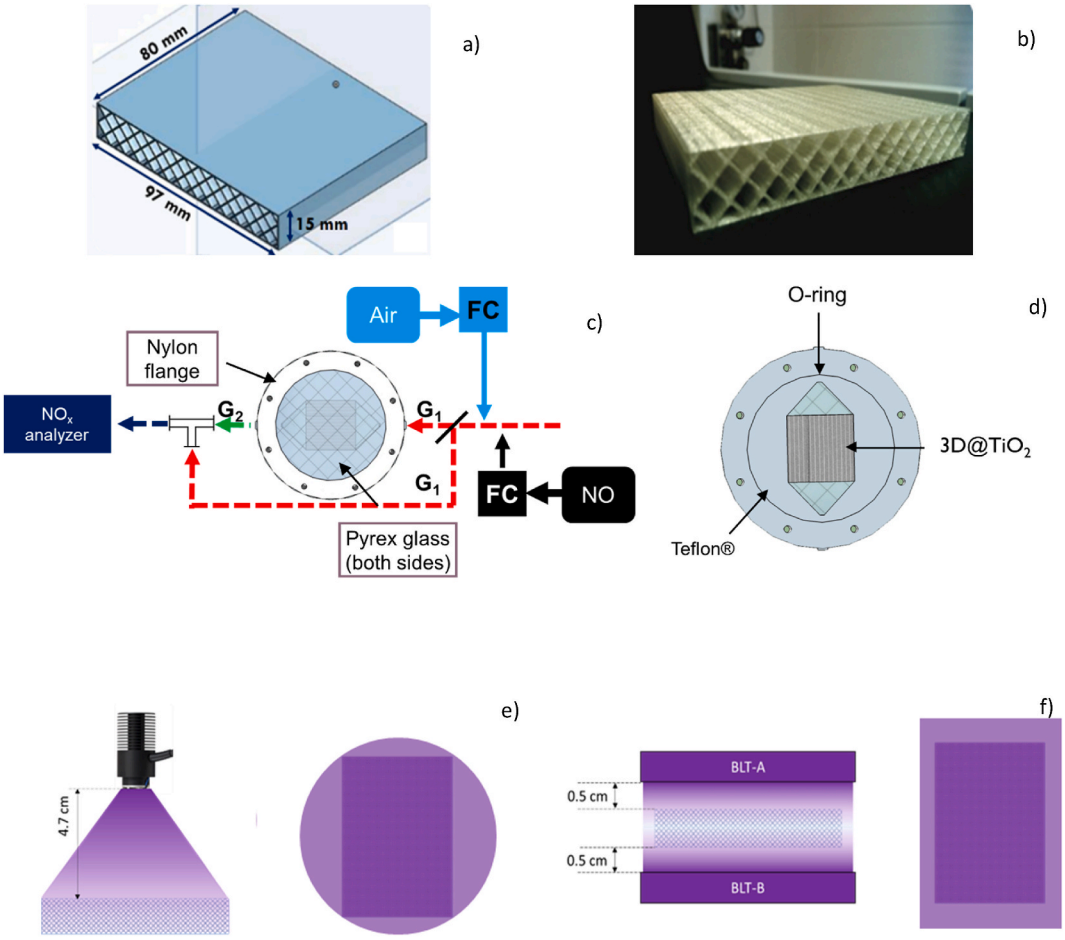

Fig. 1. a) 15% infill density monolith visualized in OnShape software; b) PET 3D-printed monolith; c) NO_x removal experimental setup (G_1: gas stream 1, NO 40 ppm; G_2: gas stream 2, treated NO; FC: Flow controller); d) Inside of the photoreactor containing the TiO_2 coated 3D printed monolith (3D@TiO_2); e) and f) irradiation setup, front and top views for Thorlabs 525 mA UV LED lamp (UVLED, $\lambda_{max} = 365$ nm) and two sets of three Yarlux T5 8 W black light tubes (BLT-A and BLT-B, $\lambda_{max} = 360$ nm), respectively.

The utilization of oxidative Heterogeneous Photocatalysis (HP) with TiO_2 has been extensively investigated for NO removal, even at industrial scales [18–21]. Moreover, the extensive knowledge gained regarding the gas-phase oxidation of NO has made it a model target for evaluating the air-purification performance of photocatalytic materials and films [22]. Guided by these model reactions and photocatalyst, we made a systematic exploration, focusing into the convergence of innovation and accessibility.

The reaction system used in this work features a reactive zone composed of TiO_2-impregnated 3D-printed polyethylene terephthalate (PET) multichannel monolith. Through methodical analysis, we examined various factors, encompassing the number of TiO_2 layers in the monoliths, the type of PET filament used, the UV light absorption properties, the UV light source, and the type of TiO_2 catalyst employed.

2. Materials and methods

2.1. Design and production of 3D-printed PET supports

Polyethylene terephthalate monoliths measuring 97 mm × 80 mm × 15 mm with transversal rhomboidal section channels were developed using the Computer-Aided Design (CAD) software OnShape (Fig. 1 a)). The monoliths were processed by the slicer software Ultimaker Cura and printed using a FDM Chimak Leon 2020 3D printer (Fig. 1 b)), following the technical specifications outlined in Table 1.

The printing parameters were selected through a "trial and error" approach, starting with the standard printing conditions recommended by PET filament suppliers. The monoliths were printed with a selected infill density of 15%. This choice was made to optimize the transmission of UV light throughout the entire height of the monolith, as explained in detail in the supporting information (see Fig. S1). Two different types of commercial PET filaments were used as printing materials: BPET (a 100% recycled filament) and PETG (a glycol-modified plastic). Fourteen monoliths, 3D-printed using either BPET or PETG, were weighed and the average weight was determined to be 35.8 ± 0.5 g. This weight is similar to the average weight of a standard 1.5 L PET carbonated drink bottle, which is approximately 32.6 g [23]. The filament consumption exhibited remarkable reproducibility, irrespective of the type of PET filament used.

2.2. Photocatalyst immobilization in supports

The 3D-printed supports were impregnated with TiO_2 by immersing them in a 900 mL crystallizer containing 800 mL of a 20 g/L TiO_2 suspension at pH 2.5 (adjusted with perchloric acid 0.05 M). Two different types of commercial TiO_2 were used for the suspension: Aeroxide P25 (provided by Evonik) and UV-100 (provided by Hombikat), depending on the specific experiment. The immersion process took place in an ultrasonic bath for 10 min. The impregnated supports were dried overnight at 50 °C inside a Vacuum DRY Box DZ-1BC and then preserved until use in a sealed bag. Supports with 1, 2 or 3 TiO_2 layers were produced by applying the aforementioned procedure consecutively. Hereafter, the TiO_2-impregnated PET supports will be referred generically as TiO_2@PET. However, when specific reference is made to P25 or UV100 or, to PETG or BPET, it will be clearly indicated in the sample name.

2.3. Characterization of PET monoliths

To study the deposition of the photocatalysts on the surface, flat test pieces of BPET measuring 20 × 20 × 1.8 mm were 3D printed and then impregnated with P25–TiO_2 following the procedure described earlier. These pieces were examined by SEM (Quanta Fei 200) employing both secondary and backscattered electrons techniques.

The textural properties of both sides of impregnated and non-impregnated flat discs were also studied by atomic force microscopy (AFM). The AFM measurements were performed with a Nanotec ELECTRONIC AFM microscope, employing a Tap190AI-G tip. The microscope was operated in tapping mode, using a silicon probe with 190 kHz resonance frequency and a constant force of 48 N/m.

UV–vis–NIR diffuse reflectance spectrometry measurements were carried out on both free and TiO_2-impregnated PET discs. The discs had a diameter of 25 mm and a thickness of 1.8 mm thick, with 100% infill density. The measurements were conducted using a Shimadzu 3600+ equipped with an integrating sphere accessory. $BaSO_4$ was utilized as the baseline standard for calibration purposes.

The UV light transmittance of the supports was studied by placing a TiO_2@PET or PET monolith at 4.5 cm from a UV LED source. The percentual transmittance was determined by employing equation [2],

Table 1
Printing parameters adopted in Ultimaker Cura slicer.

Wall Thickness	1 mm
Wall Line Count	1
Top/Bottom Layers	0
Infill Density	15%
Printing Temperature	240 °C
Build Plate Temperature	70 °C
Print Speed	45 mm/s
Build Plate Adhesion Type	BRIM 5 mm
Filament Type	PET

$$T\,(\%) = 100 \times \frac{I}{I_0} \quad [2]$$

where, I represents the average 365 nm photon irradiance through the monoliths, while I_0 the corresponds to the average 365 nm photon irradiance at the same distance from the source but in the absence of the monoliths. The irradiance measurements were conducted using a Spectroline Model DM-365 XA radiometer.

2.4. NO_x removal experiments

NOx removal experiments were carried out using an experimental setup depicted in Fig. 1 c) and d) which comprises a PTFE flat continuous flow gas phase reactor with two Pyrex glass tops, which act as glass windows. These glass windows seal the TiO_2-impregnated support inside the reactor (more detail in Figures S1 c) and d)). A gaseous stream of NO at a concentration of 40 ppm was generated by online mixing of a concentrated NO stream (provided by Linde) with clean, dry air from an air compressor provided by ICON Argentina. The cylinder containing concentrated NO consisted of a mixture of 1000 ppm NO and N_2, with 5% NO_2. As a result, the gas stream entering the reactor at the inlet had 2.5 ppm of NO_2. This NO stream was introduced into the reactor at a flow rate of 600 mL/min, equivalent to a total space time of 15 s. Prior to turning on the lights, the NO stream was passed through the reactor during 5 min. In the absence of light, no occurrences of NO_2 or NO removal associated with thermal adsorption was observed in any of the experiments carried out in this work. Subsequently, each experiment underwent a continuous 3-h exposure to UV light at an average constant temperature of 25 °C. The effect of water presence during the reaction was investigated through an experiment with relative humidity (RH) set at 95%. This RH level was reached by continuous bubbling of the dry air stream into MilliQ water at 25 °C. During each experiment, the concentrations of NO, NO_2 and NO_x were continuously monitored by using a Teledyne T-200 M NO_x analyzer. The concentration profiles were processed using the associated APICOM software. Each experiment was performed in duplicate.

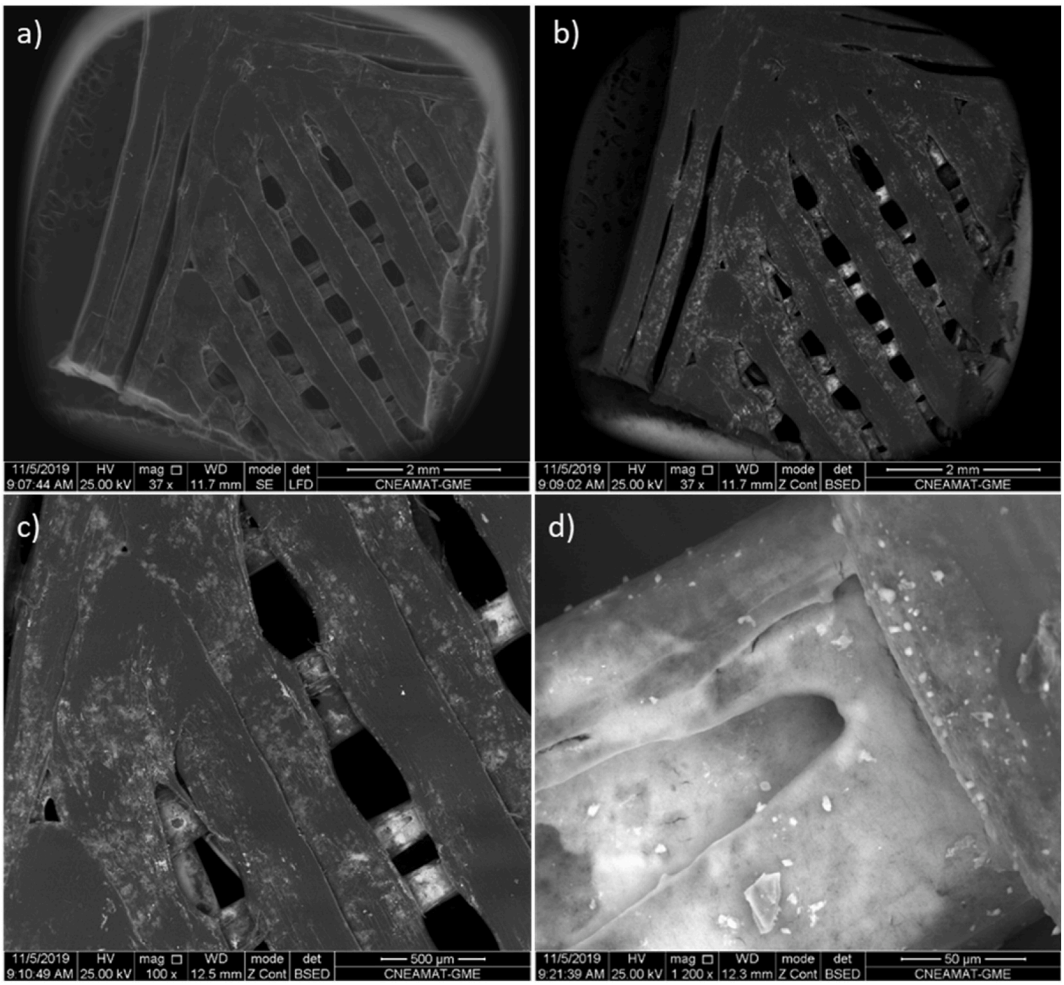

Fig. 2. Secondary electrons a) and backscattered electrons b), c) and d) SEM images of PETG 3D printed pieces impregnated with P25.

The removal efficiency (R^X) of NO and NO_x per mass of photocatalyst was calculated in μmol of each species per gram of TiO_2 by integrating the time-resolved concentration profiles of NO or NO_x during the experiments, as per equation [3]. The selectivity of the photocatalytic process towards the formation of nitrate was calculated using equation [4], which involves the ratio between the removal efficiencies of NOx and NO. Finally, a $DeNO_x$ index (R^{DeNOx}, equation [5]) constructed based on the work of Bloh et al. [18] was also calculated to quantify the effective toxicity reduction achieved in each explored condition.

$$R^X = \frac{Q}{m \times \varphi} \times \int_{t_0}^{t_f} [X]_0 - [X]dt \quad [3]$$

$$S = 100 \times \frac{R^{NO_x}}{R^{NO}} \quad [4]$$

$$R^{DeNOx} = R^{NO_x}\left(3 - \frac{2 \times 100}{S}\right) \quad [5]$$

where m is the mass of photocatalyst in the supports (g), Q is the volumetric flow rate (L/min), φ is the ideal molar volume (L/mol) and $[X]$ and $[X]_0$ are, respectively, the time resolved and initial concentration of NO or NO_x (ppmv).

The experiments were performed using either a Thorlabs 525 mA UV LED lamp (UVLED) or two sets of three Yarlux T5 8 W black light tubes (BLT-A and BLT-B) as UV light sources AB. Both UV light sources present a unique emission peak with a maximum centered

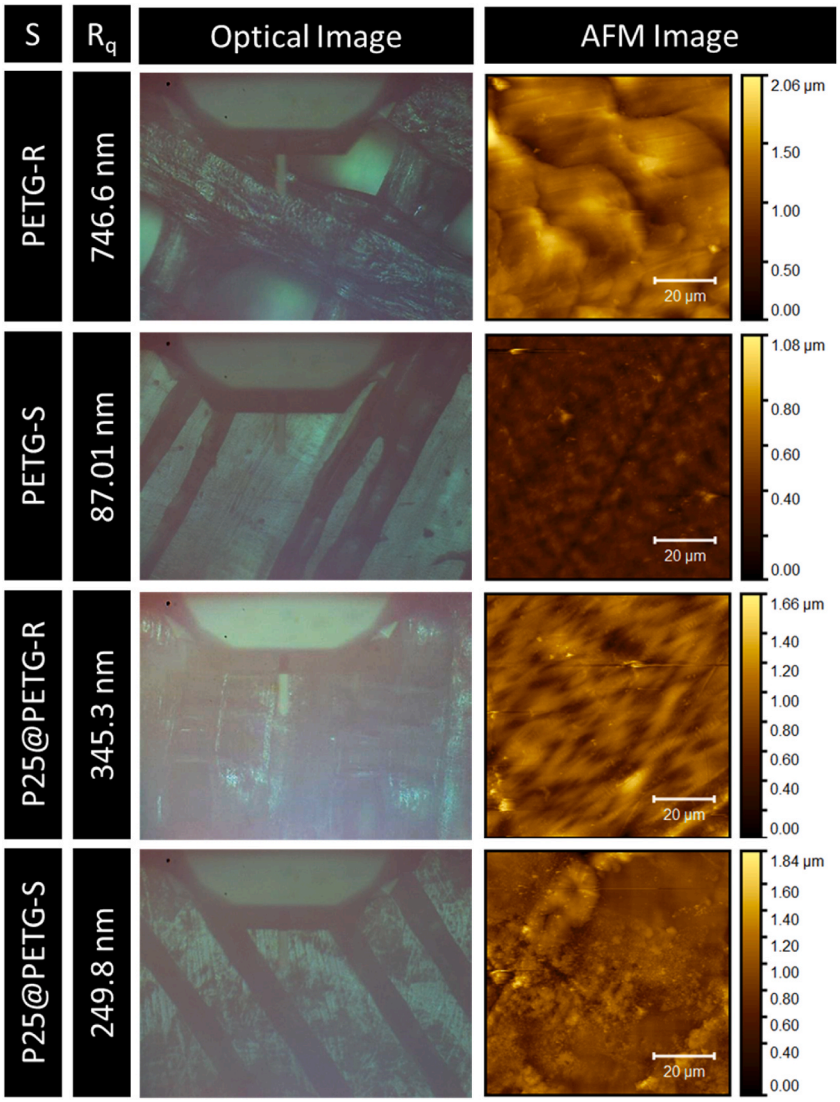

Fig. 3. R_q values, optical and AFM images for PET and P25@PET on both sides: rough (R) and smooth (S).

in 365 nm. For the UVLED, it was positioned at 4.7 cm from one of the glass windows of the reactor, resulting in a measured irradiance of 3300 μW/cm^2. On the other hand, for each set of BLT, they were placed at a distance of 0.5 cm, effectively irradiating both glass windows. The measured irradiances for BLT-A and BLT-B were 1374 and 2401 μW/cm^2, respectively. The distance of each UV light source to the reactor glass window was selected to maximize the coverage of the monolith area by the light. Both configurations are illustrated in Fig. 1 e) and f).

3. Results and discussion

3.1. Characterization of impregnated and non-impregnated supports

Fig. 2 a) and c) present the SEM images of a flat impregnated monolith where only the first two filament layers can be observed. The filaments are observed to be organized in layers, which aligns with the expected arrangements resulting from the printing technique used. The printing pattern of the monolith involved 90° rotated layers of parallel filaments. The top layer of the monolith exhibited fused and overlapped filaments of 366 ± 42 μm in thickness but in the second deeper filament layer, the PET threads have a thickness of 215 ± 39 μm. The general aspect of the top layer can be attributed to filament flattening, a phenomenon commonly observed in the first printed layer by FDM that directly contacted the glass platform of the 3D printer. This irregularity becomes less pronounced and is reduced to a minor boundary effect as the following layers are printed.

Secondary electron SEM images (Fig. 2 b) and d)) show the zones where the TiO_2 deposition occurs, with the TiO_2 distribution following the irregular morphology of the printed object. The contrast achieved through this technique provides clear differentiation between regions that are heavily covered by TiO_2 and those that are less covered, thereby highlighting the irregular micrometric structure of the base polymer filaments intersected by striations where the photocatalyst accumulates.

The AFM images of the impregnated and native PET flat pieces are presented in Fig. 3. The optical images clearly indicate a noticeable difference between the two sides of each PET flat piece, with one side appearing smoother in texture. The rougher side corresponds to the last layer of filament printed, whereas the smoother corresponds to the first printed PET layer that acquires a glassy appearance as the molten filaments flatten upon contact with the glass surface during fused extrusion before solidifying. AFM images also demonstrate the disparity in surface rugosity between both sides of each material. It is worth noting that the presence of TiO_2 nanoparticles was primarily evident in the case of P25@PET-S flat piece. Sample P25@PET-R present randomly distributed clusters that may potentially consist of TiO_2 nanoparticles agglomerates. However, it is important to note that similar formations can also be observed in samples PET-S and PET-R, which could be attributed to dust particles or irregularities in the PET material. The analysis of the mean square root roughness (R_q), as shown in Fig. 3 revealed an indirect effect of coating the PET filament with TiO_2. Specifically, it was observed that the roughness of the rough side of the P25@PET flat piece decreased as the surface cavities were filled with the photocatalyst nanoparticles. Consequently, the presence of surface TiO_2 agglomerates led to an increase in the roughness of the smooth side. These observations are consistent with the findings from the SEM analysis.

Fig. 4 a) depicts the absorbance spectra of PET, P25 powder and PET disc impregnated with P25 (P25@PET) samples. PET and P25 were observed to absorb light at $\lambda < 404$ nm with distinct absorption patterns. The combination of these patterns is clearly observed in the P25@PET spectrum. PET exhibit a gradual increase in absorption as the wavelength decreases from 404 nm to 334 nm and then it steeply increases from that point for lower values of λ. On the other hand, P25 shows a rapid increase in absorption from around 404 nm to 332 nm. The spectrum of P25@PET clearly indicates the effective impregnation of PET, as it represents the combined spectra of P25 and PET also evidenced by the presence of a shoulder with an apparent maximum centered in 346 nm.

The inserted figure in Fig. 4 represent the near-infrared (NIR) absorption profile for PET and P25@PET. The absorbance peaks of the polymer can be grouped in three regions: region 1 (1200–1400 nm), region 2 (1550–1850 nm) and region 3 (1850–2000 nm) [24].

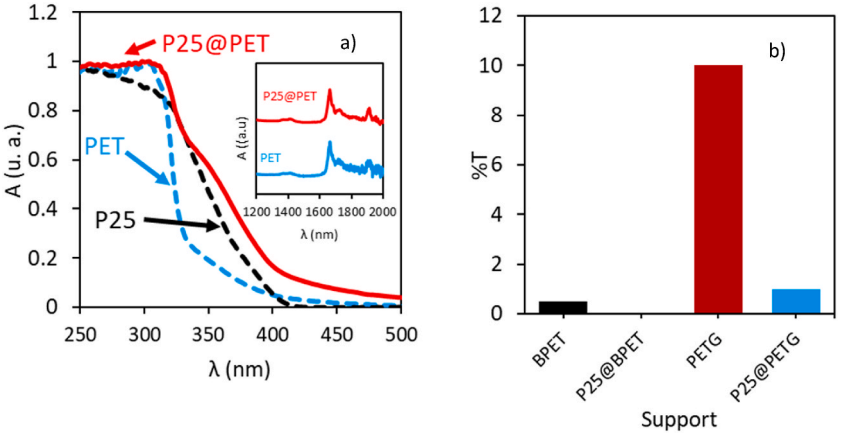

Fig. 4. a) Normalized absorbance spectra of PET and P25@PET discs and P25 powder; b) %T of impregnated an unimpregnated PETG and BPET printed supports at 365 nm.

Regions 1 and 2 contain a combination of first and second-overtone bands from aromatic C–H groups in the terephthalic acid part and methylene groups in the ethylene glycol part. Region 3 contains the second-overtone carbonyl stretching band and absorbances from moisture in the polymer. There was no evident change in the NIR peak distribution after P25 impregnation.

The transmittance of PETG, PETG with 1 layer of TiO_2 and BPET was measured. As can be observed in Fig. 4 b), all the monoliths are capable of transmitting a portion of the incident light from the UV LED light source. Nevertheless, the monoliths produced using PETG filament resulted significantly more transparent to UV light than the ones built with BPET. PETG and pure PET polymers have been shown to have similar optical density in comparative studies, as demonstrated by Cámara et al. [25]. Therefore, the difference in %T between these materials could be attributed to a higher roughness of the extruded filament in the BPET-made monoliths. In addition, it is worth noting that the addition of 1 layer of P25 significantly decreases the %T at 365 nm due to the light absorption of the photocatalyst throughout the impregnated monolith structure.

3.2. Removal of NOx

3.2.1. NOx removal profile, mechanism, and water effect

Fig. 5 a) shows the concentration profiles of NO, NO_x and NO_2 at the outlet of the reactor during UV LED light irradiation and depicts a typical time-resolved concentration profile. Prior to initiating the reaction by turning on the light, NO gas flowed through the reactor in the dark to ensure saturation of the photocatalyst surface.

In a typical time resolved concentration profile as the one depicted in Fig. 5 a), NO and NO_x concentrations exhibit a rapid decrease within the first 5 min after turning on the UV-light source. Subsequently, the concentration shows a gradual increase over the duration of the experiment, eventually reaching a steady-state regime. Once the UV lights were turned off, the initial concentration values of NO and NO_x were observed to recovered. The highest value of selectivity towards nitrate is observed at 5 min of UV irradiation, which is expected as at that point the generation of NO_2 is negligible and NO is the primary compound undergoing reaction.

$$H_2O + h^+_{bv} \rightarrow HO^\bullet + H^+ \quad [6]$$

$$O_2 + e^-_{cb} + H^+ \rightarrow HO^\bullet_2 \quad [7]$$

$$HO^\bullet_2 + e^-_{cb} + H^+ \rightarrow H_2O_2 \quad [8]$$

$$H_2O_2 + e^-_{cb} + H^+ \rightarrow HO^\bullet + H_2O \quad [9]$$

$$HO^\bullet + e^-_{cb} + H^+ \rightarrow H_2O \quad [10]$$

The photocatalytic oxidation of NO to nitrate is a reaction principally mediated by $OH^\bullet$ radicals. Initially, $OH^\bullet$ are formed through the reaction between water adsorbed on the photocatalyst surface and photogenerated holes (equation [6]). These $OH^\bullet$ radicals then react rapidly with adsorbed NO, resulting in HONO formation. The conversion of HONO to NO_2 occurs at a slower rate, leading to the establishment of the initial kinetic regime [26]. As previously stated by Folli et al. [27], the photocatalytic oxidation of NO is indeed a water-content dependent reaction. When the availability of adsorbed water is reduced, the production of HONO decreases, becoming the limiting step of the photocatalytic oxidation process. This, together with surface deactivation after the irreversible adsorption of nitrates, ultimately leads to a decrease in NO and NO_x conversions. Fig. 5 (b) shows the removal efficiency per mass of photocatalyst (R^{NO} and R^{NOx}) obtained for both humid and dry air conditions. The findings provide compelling evidence of the crucial role of water in this photocatalytic process. The results clearly evidence that the continuous supply of water into the reactor (RH = 95%) leads to significantly higher values for R^{NO} and R^{NOx} compared to when dry air is used (RH = 0%). In fact, the observed values of R^{NO} and R^{NOx} are more than two times higher in the presence of water. Given that water molecules are crucial for generating $OH^\bullet$ radicals and sustaining the photocatalytic circuit through hole capturing, a continuous water supply into the reactor should always lead to improve NO conversion efficiency. For instance, a study conducted by Devahasdin et al. [26] provide empirical evidence of the interplay

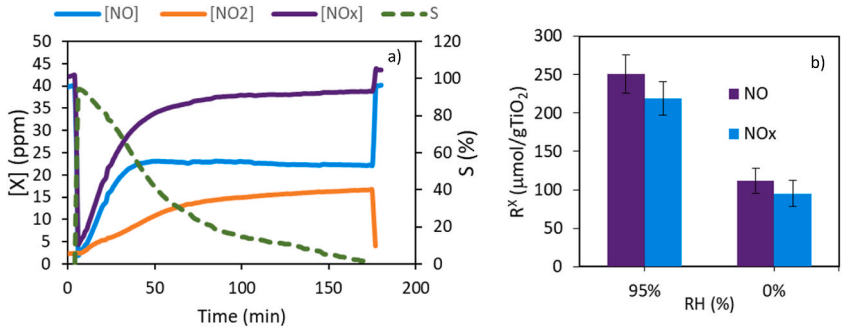

Fig. 5. a) NO, NO_x and NO_2 concentration profiles and time resolved selectivity (S) during the photocatalytic removal of NO (during the first and last 5 min the lights are turned off) with UV100 over PETG using two sets of BLTs; b) R^x for 1 layer of TiO_2 run with P25@BPET and UV-LED under humid air (RH = 95%) and dry air (RH = 0%).

between water content and NO conversion efficiency. The researchers investigated the conversion of a gas stream containing 40 ppm of NO under the effect of varying gaseous water content. As RH increased from 0 to 50% the NO conversion scaled from 5% to 35%, remaining in 35% beyond 50% of RH. However, the relationship between water and NO conversion is not uniform across different scenarios. In a recent review published by Rhimi et al. [20] the authors point out that for feeding NO concentrations in the ppb level increasing H_2O molecules strongly competes for the adsorption sites while NO loaded gas streams in the ppm level benefit from an increasing amount of water as NO molecules adsorption is evidently favored against H_2O.

Afterwards, NO and NO_x conversions decrease as the production of HONO becomes the limiting step due to surface hydration water consumption and to surface deactivation after the irreversible adsorption of nitrates, leading to an increase in NO_2 production.

Through the capture of conduction band electrons, molecular oxygen reduction can lead to the formation of hydroperoxyl radical or hydrogen peroxide (equations [7,8]). These species are capable of oxidizing NO, resulting in the production of NO_2 and HONO, respectively. However, this pathway can be kinetically limited when considering pure TiO_2. In the most extreme scenario, O_2 conversion to water could occur upon the capture of four conduction band electrons (equations [9,10]). Consequently, this pathway significance is likely to take place predominantly under conditions characterized by a limited presence of adsorbed water [28]. Furthermore, Patzsch et al. [29], demonstrated the critical role of reaction with O_2 in achieving complete mineralization of NO. They emphasized that this pathway significantly influences NO_x selectivity as it competes with back-reduction reactions of nitrates, ultimately leading to the release of NO_2 [30].

3.2.2. *Effect of the amount of TiO_2 layers*

In order to investigate the influence of the number of TiO_2 layers on NO_x removal, a series of experiments were carried out using supports with varying numbers of TiO_2 layers (1, 2, and 3). The results shown in Fig. 6 clearly indicate that increasing the number of TiO_2 layers from 1 to 3 had a counterproductive effect on the removal efficiency. The results demonstrated a reduction in R^{NOx} of 23% and 30% when utilizing supports with 2 and 3 TiO_2 layers, respectively. The decrease in removal efficiency observed when employing multiple layers of photocatalyst can be attributed to the limited increase in active sites after the deposition of new TiO_2 over the previous layers. As a result, the retained photocatalyst is not effectively used, leading to a decrease in the removal efficiency defined per mass of TiO_2. This analysis is supported by the results shown in Fig. S2 (supporting information), where it can be observed that the total amount of NO_x and NO removed does not significantly change with an increase in the TiO_2 amount (higher number of TiO_2 layers).

Lopes Barros et al. [31] reported similar findings in their study on the photocatalytic removal of paracetamol using TiO_2 impregnated PET stripes obtained from drink bottles. They observed that after 5 to 15 PET impregnation runs using a similar impregnation methodology to this work, there was no further change in the apparent paracetamol removal rate constant. This coincidental behavior for different systems suggests that the impregnation protocol should be optimized. One possible approach is to explore the effect of lower TiO_2 suspension concentrations during the immersion of PET pieces. Following this finding, supports impregnated with only one layer of TiO_2 were selected for the subsequent experiments. This choice was made to ensure maximum R^{NO} and R^{NOx} values, allowing for a focused exploration of other key factors affecting the photocatalytic performance of the system. It is worth mentioning that the high level of durability demonstrated by the monoliths during the impregnation process makes them suitable for periodic re-impregnation with TiO_2. This process could help to restore their catalytic activity, given that nitrate is irreversibly adsorbed onto the surface.

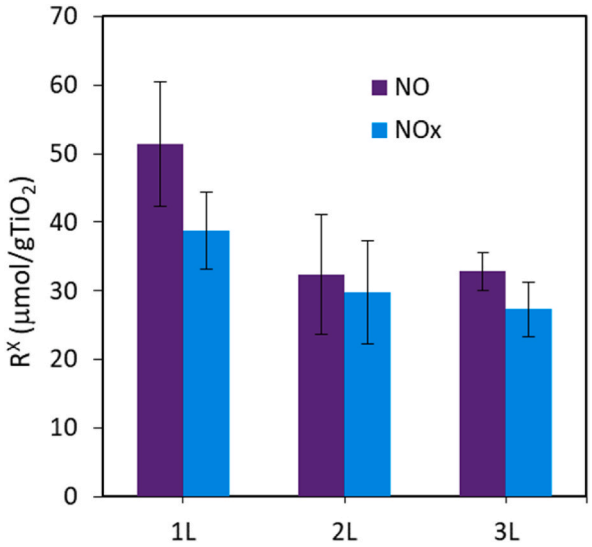

Fig. 6. R^x for 1 (1 L), 2 (2 L) or 3 (3 L) TiO_2 layers after each impregnation run with P25@BPET and UV-LED irradiation.

3.2.3. Effect of filament composition

Fig. 7 shows the removal efficiency per mass of photocatalyst using BPET and PETG 3D-printed monoliths impregnated with P25. PETG presented a notable increase of 117% in R^{NO} and 146% in R^{NOx}, compared to BPET. The higher R^{x} values can be attributed to the fact that monoliths 3D-printed with BPET filament retained nearly twice the amount of TiO_2 compared to those using PETG. This difference in TiO_2 retention could be ascribed to the higher roughness of the BPET filament, which is consistent with the lower transmittance observed for the unimpregnated monolith in Fig. 4 b). In fact, the net amount of NO and NO_x removed by both types of PET-constructed monoliths does not differ significantly (Fig. S3); once again, the TiO_2 excess retained in each monolith resulted in a saturated photocatalytic performance. Therefore, the use of BPET results in a much attractive choice of filament from an environmental perspective, as the polymer presents fairly stable optical properties after up to 11 cycles simulating recycling and production process [32].

3.2.4. Effect of UV light source

Fig. 8 shows the removal efficiency per mass of photocatalyst using both UV LED irradiation and the two sets of black light lamps as UV light sources. The NO_x removal (R^{NO} and R^{NOx}) achieved with the BLTs was three times higher compared to that obtained with the LED light lamp despite the total irradiance difference between BLT-A + BLT-B (3775 μW/cm^2) and UV-LED (3300 μW/cm^2) being only 15% higher. This highlights the importance of the irradiation distribution. The radiant power decreases as light passes through the PET structures and/or the TiO_2 impregnated nanoparticles. However, by irradiating both sides of the reactor, a more uniform and higher intensity illumination is achieved inside each monolith. This allows for a greater utilization of the light, resulting in an enhanced overall performance compared to single-sided irradiation.

3.2.5. Effect of TiO_2 type

UV100-impregnated supports exhibited a twofold increase in R^{NOx} and a fourfold increase in R^{NO} compared to the supports impregnated with P25, as shown in Fig. 9. UV100 showed higher removal efficiency for both NO_x and NO throughout the entire duration of the experiment, as depicted in Fig. S4. A similar result was reported by Hernández Rodríguez et al. [33] demonstrating that the photocatalyst surface area had the greatest impact on the final product yield.

UV100 exhibits a specific surface area that is approximately five times larger than that of P25 [34] (Table S1). Additionally, according to the work of Nosaka et al. [35] UV100 has nearly 60% more water adsorbed per surface area. Based on the TiO_2 retention measurements, PETG monoliths impregnated with P25 and UV100 retained 0.117 ± 0.005 and 0.0602 ± 0.006 g of TiO_2, respectively. This indicates that UV100@PETG provides around 4 times more surface water molecules than P25@PETG. This higher availability of surface water molecules can explain the enhanced performance observed with UV100@PETG. In agreement with the arguments presented by Folli et al. [27], a higher initial NO removal rate also leads to a lower selectivity due to the rapid depletion of surface available water molecules. This depletion leads to photocatalyst deactivation and higher production of NO_2.

3.2.6. Removal efficiency, selectivity and denoxification

Direct performance comparison on NO_x removal poses challenges due to variations in reactor configurations, different irradiation systems, and limited availability of comprehensive experimental details in previous studies. Hence, the choice of an appropriate index is necessary for facilitating accurate assessments. In our work, we selected a removal efficiency definition that considers the overall NO_x and NO removed over a 3-h period, including the peak performance during the first minutes of operation. For instance, the same

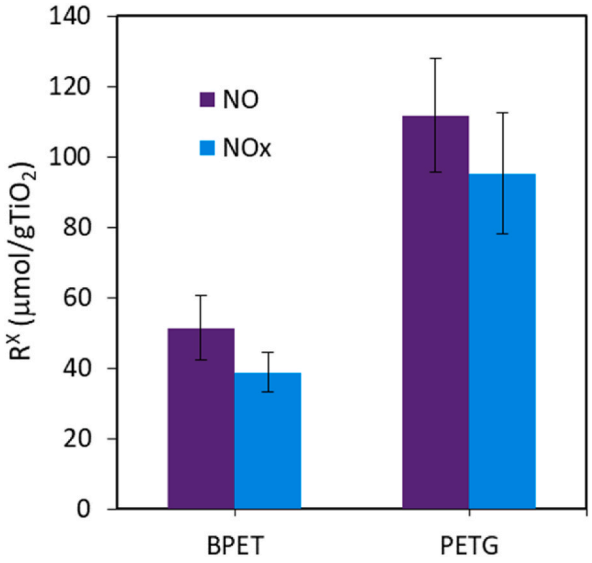

Fig. 7. R^{x} for 1 L P25@BPET and P25@PETG and UV-LED irradiation.

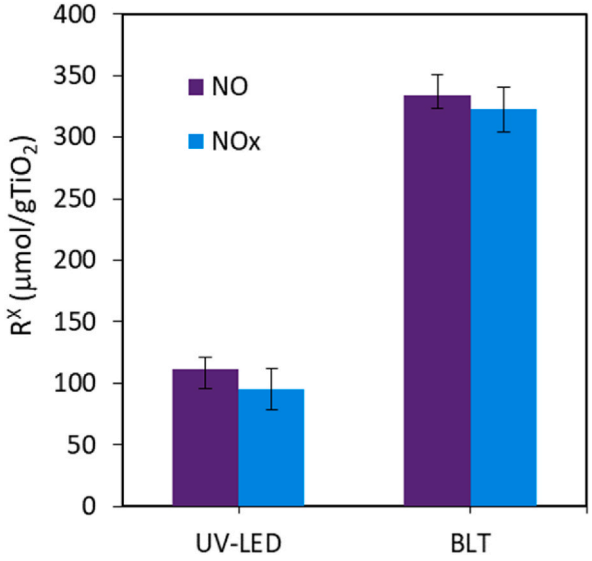

Fig. 8. R^x for 1 L P25@PETG using the two irradiation setups (UVLED and BLT).

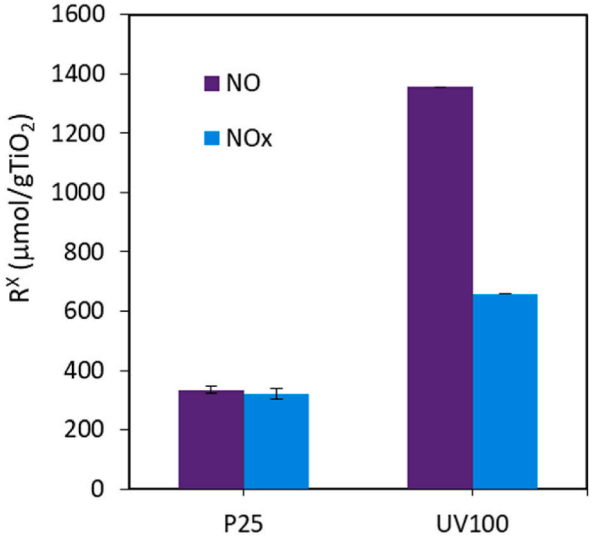

Fig. 9. R^x for 1 L P25@PETG and 1 L UV100@PETG.

approach was used by Hu et al. [36] who utilized a much expensive and complex experimental arrangement. Their setup comprises a flat quartz reactor containing dispersed powdered photocatalysts at the base, subjected to irradiated from above with a high-pressure mercury lamp. The authors reported a NO removal efficiency of 118 µmol/g of P25 and a NO_x removal efficiency of 25 µmol/g of P25 in 1 h for a feeding gas stream containing 40 ppm of NO (RH = 70%, T = 80 °C). In terms of global performance, these results are in the same range than the maximum values for R^{NO} and R^{NOx} obtained in this work for P25@PETG irradiated with 2BLT under RH = 0%: 334 µmol/g of P25 and 322 µmol/g of P25, respectively.

Bloh et al. [18] highlighted that NO_2 has a relative toxicity that is 8–25 times higher compared to NO, suggesting that in scenarios where photocatalyst selectivity is low, there is a potential for increased toxicity of a NO_x gas stream. To effectively evaluate the removal of NO_x photocatalysts, considering both their activity and selectivity, the authors introduced a DeNOx index. When the DeNOx index takes positive values, it indicates that the photocatalyst effectively reduces the toxicity of the gas stream. A selectivity of at least 66.7% serves as the threshold for a positive DeNOx index. Even though the overall selectivity calculation performed by Bloh slightly underestimates the conversion of NO and NO_x as it focuses in the steady-state concentration values instead of integrating the concentration profile curves the use of the DeNOx index remains a very useful parameter for evaluating the improvement in the quality of the outlet stream in terms of toxicity. Using the DeNOx index as a reference, as shown in Table S2, under the investigated experimental conditions, it was observed that only P25 could decrease the toxicity of the original 40 ppm NO gas stream. Regardless of the

UV-light source, the filament, or the number of layers P25 takes always positive values of R^{DeNOx}, while UV100 yielded an overall negative R^{DeNOx} quantitatively attributable to a lower selectivity evidence by UV100; the selectivity was higher than 71% for P25 and 43.9% for UV100. These values differ from those obtained by Bloh et al. [18] which reported a selectivity of 27.8% for P25 and of 27.2% for UV100. While this divergence for each photocatalyst still remains unclear, these values may be influenced by evident differences in the gas flow rate and residence time, mass of catalyst used and the irradiance of the light sources, among others.

4. Conclusions

NO_x removal via heterogeneous photocatalysis was successfully achieved using impregnated TiO_2 on 3D printed PET monoliths. We investigated various key factors known to impact photocatalytic NO_x removal, including the presence of water, type of photocatalyst, and irradiation setup. Additionally, specific variables associated with the use of FDM as a construction technique, such as infill density and the type of feedstock filament, were also explored. The experimental conditions that yielded the highest removal efficiency of NO_x were found to be the use of PETG as the printing material, a single layer of TiO_2 impregnation, irradiation of both sides of the photoreactor, and continuous water supply. Regarding the effect of the type of photocatalyst, UV100 demonstrated a much higher removal efficiency compared to P25, even though a low selectivity towards nitrate was observed under the studied conditions. However, it is important to note that the selectivity can be improved by optimizing the operative conditions of the process.

These results underscore the strength and simplicity of 3D-printed supports as a viable tool for the versatile design of photocatalytic systems used in the removal of gaseous pollutants. Furthermore, this work also shows that 3D printing is a promising way for building photocatalytic supports with high reproducibility and low environmental impact when recycle PET is used as feedstock filament.

Our work contributes to the ongoing conversation surrounding the application of 3D printing in photocatalytic reactor design. We acknowledge the promise held by the 3D printing approach, which, when combined with photocatalysis, holds the potential to reshape the landscape of gaseous pollutant removal with both efficacy and environmental responsibility.

Data availability statement

Data associated with this study has not been deposited into a publicly available repository, but it will be made available on request.

CRediT authorship contribution statement

G.F. Binetti Basterrechea: Writing – original draft, Investigation, Formal analysis. **V.N. Montesinos:** Writing – review & editing, Supervision, Project administration, Methodology, Conceptualization. **N. Quici:** Writing – review & editing, Project administration, Methodology, Funding acquisition, Conceptualization.

Declaration of competing interest

The authors declare that they have no known competing financial interests or personal relationships that could have appeared to influence the work reported in this paper.

Acknowledgements

The authors thank their corresponding institutions,as well asPhosAgro, UNESCO, IUPAC, UTN, and CONICET for their finantial support. Dr. Montesinos and Dr. Quici would also thank to Guido Palazzo for his input and advice on 3D designing and printing.

Appendix A. Supplementary data

Supplementary data to this article can be found online at https://doi.org/10.1016/j.heliyon.2023.e22635.

References

[1] C. Parra-Cabrera, C. Achille, S. Kuhn, R. Ameloot, 3D printing in chemical engineering and catalytic technology: structured catalysts, mixers and reactors, Chem. Soc. Rev. 47 (2018) 209–230, https://doi.org/10.1039/c7cs00631d.
[2] D. Friedmann, A.F. Lee, K. Wilson, R. Jalili, R.A. Caruso, Printing approaches to inorganic semiconductor photocatalyst fabrication, J Mater Chem A Mater 7 (2019) 10858–10878, https://doi.org/10.1039/C9TA00888H.
[3] M.R. Hartings, Z. Ahmed, Chemistry from 3D printed objects, Nat. Rev. Chem 3 (2019) 305–314, https://doi.org/10.1038/s41570-019-0097-z.
[4] M.R. Skorski, J.M. Esenther, Z. Ahmed, A.E. Miller, M.R. Hartings, The chemical, mechanical, and physical properties of 3D printed materials composed of TiO 2 -ABS nanocomposites, Sci. Technol. Adv. Mater. 17 (2016) 89–97, https://doi.org/10.1080/14686996.2016.1152879.
[5] M.D. Symes, P.J. Kitson, J. Yan, C. Richmond, G.J.T. Cooper, R.W. Bowman, T. Vilbrandt, L. Cronin, Integrated 3D-printed reactionware for chemical synthesis and analysis, Nat. Chem. 4 (2012) 349–354, https://doi.org/10.1038/nchem.1313.
[6] P.J. Kitson, M.D. Symes, V. Dragone, L. Cronin, Combining 3D printing and liquid handling to produce user-friendly reactionware for chemical synthesis and purification, Chem. Sci. 4 (2013) 3099–3103, https://doi.org/10.1039/c3sc51253c.

[7] L.J. Frey, D. Vorländer, H. Ostsieker, D. Rasch, J.-L. Lohse, M. Breitfeld, J.-H. Grosch, G.D. Wehinger, J. Bahnemann, R. Krull, 3D-printed micro bubble column reactor with integrated microsensors for biotechnological applications: from design to evaluation, Sci. Rep. 11 (2021) 7276, https://doi.org/10.1038/s41598-021-86654-9.

[8] J. Zhu, P. Wu, Y. Chao, J. Yu, W. Zhu, Z. Liu, C. Xu, Recent advances in 3D printing for catalytic applications, Chem. Eng. J. 433 (2022), https://doi.org/10.1016/j.cej.2021.134341.

[9] N. Li, K. Tong, L. Yang, X. Du, Review of 3D printing in photocatalytic substrates and catalysts, Mater. Today Energy 29 (2022), 101100, https://doi.org/10.1016/j.mtener.2022.101100.

[10] S. Govender, H.B. Friedrich, Monoliths: a review of the basics, preparation methods and their relevance to oxidation, Catalysts 7 (2017), https://doi.org/10.3390/catal7020062.

[11] M.L. Comroe, K.W. Kolasinski, D. Saha, Direct ink 3D printing of porous carbon monoliths for gas separations, Molecules 27 (2022), https://doi.org/10.3390/molecules27175653.

[12] B. Verougstraete, D. Schuddinck, J. Lefevere, G.V. Baron, J.F.M. Denayer, A 3D-printed zeolitic imidazolate framework-8 monolith for flue- and biogas separations by adsorption: influence of flow distribution and process parameters, Frontiers in Chemical Engineering 2 (2020), https://doi.org/10.3389/fceng.2020.589686.

[13] H. Thakkar, S. Eastman, Q. Al-Naddaf, A.A. Rownaghi, F. Rezaei, 3D-Printed metal-organic framework monoliths for gas adsorption processes, ACS Appl. Mater. Interfaces 9 (2017) 35908–35916, https://doi.org/10.1021/acsami.7b11626.

[14] M.A. Ávila-López, T.E. Lara-Ceniceros, F.E. Longoria, A.A. Elguezabal, A. Martínez de la Cruz, M.A. Garza-Navarro, J. Bonilla-Cruz, Photodegradation of air and water contaminants using 3D-printed TiO $_2$ nanoparticle scaffolds, ACS Appl. Nano Mater. 5 (2022) 11437–11446, https://doi.org/10.1021/acsanm.2c02498.

[15] A. Sangiorgi, Z. Gonzalez, A. Ferrandez-Montero, J. Yus, A.J. Sanchez-Herencia, C. Galassi, A. Sanson, B. Ferrari, 3D printing of photocatalytic filters using a biopolymer to immobilize TiO 2 nanoparticles, J. Electrochem. Soc. 166 (2019) H3239–H3248, https://doi.org/10.1149/2.0341905jes.

[16] A. Zhakeyev, M.C. Jones, C.G. Thomson, J.M. Tobin, H. Wang, F. Vilela, J. Xuan, Additive manufacturing of intricate and inherently photocatalytic flow reactor components, Addit. Manuf. 38 (2021), https://doi.org/10.1016/j.addma.2020.101828.

[17] V.-H. Nguyen, B.-S. Nguyen, C.-W. Huang, T.-T. Le, C.C. Nguyen, T.T. Nhi Le, D. Heo, Q.V. Ly, Q.T. Trinh, M. Shokouhimehr, C. Xia, S.S. Lam, D.-V.N. Vo, S. Y. Kim, Q. Van Le, Photocatalytic NOx abatement: recent advances and emerging trends in the development of photocatalysts, J. Clean. Prod. 270 (2020), 121912, https://doi.org/10.1016/j.jclepro.2020.121912.

[18] J.Z. Bloh, A. Folli, D.E. Macphee, Photocatalytic NO x abatement: why the selectivity matters, RSC Adv. 4 (2014) 45726–45734, https://doi.org/10.1039/C4RA07916G.

[19] T. Maggos, J.G. Bartzis, M. Liakou, C. Gobin, Photocatalytic degradation of NOx gases using TiO2-containing paint: a real scale study, J. Hazard Mater. 146 (2007) 668–673, https://doi.org/10.1016/j.jhazmat.2007.04.079.

[20] B. Rhimi, M. Padervand, H. Jouini, S. Ghasemi, D.W. Bahnemann, C. Wang, Recent progress in NOxphotocatalytic removal: surface/interface engineering and mechanistic understanding, J. Environ. Chem. Eng. 10 (2022), https://doi.org/10.1016/j.jece.2022.108566.

[21] J. Chen, C.S. Poon, Photocatalytic construction and building materials: from fundamentals to applications, Build. Environ. 44 (2009) 1899–1906, https://doi.org/10.1016/j.buildenv.2009.01.002.

[22] V. Muñoz, C. Casado, S. Suárez, B. Sánchez, J. Marugán, Photocatalytic NOx removal: rigorous kinetic modelling and ISO standard reactor simulation, Catal. Today 326 (2019) 82–93, https://doi.org/10.1016/j.cattod.2018.09.001.

[23] M.S. Islam, Plastic waste and carbon footprint generation due to the consumption of bottled waters in Saudi arabia, Res. Dev. Mater. Sci. 5 (2018), https://doi.org/10.31031/rdms.2018.05.000604.

[24] C.E. Miller, B.E. Eichinger, Determination of crystallinity and morphology of fibrous and bulk poly(ethylene terephthalate) by near-infrared diffuse reflectance spectroscopy, Appl. Spectrosc. 44 (1990) 496–504, https://doi.org/10.1366/0003702904086173.

[25] R.M. Cámara, R. Portela, F. Gutiérrez-Martín, B. Sánchez, Photocatalytic activity of TiO2 films prepared by surfactant-mediated sol–gel methods over commercial polymer substrates, Chem. Eng. J. 283 (2016) 535–543, https://doi.org/10.1016/j.cej.2015.07.080.

[26] S. Devahasdin, C. Fan, K. Li, D.H. Chen, TiO2 photocatalytic oxidation of nitric oxide: transient behavior and reaction kinetics, J. Photochem. Photobiol. Chem. 156 (2003) 161–170, https://doi.org/10.1016/S1010-6030(03)00005-4.

[27] A. Folli, S.B. Campbell, J.A. Anderson, D.E. Macphee, Role of TiO2 surface hydration on NO oxidation photo-activity, J. Photochem. Photobiol. Chem. 220 (2011) 85–93, https://doi.org/10.1016/j.jphotochem.2011.03.017.

[28] A. Folli, J.Z. Bloh, K. Armstrong, E. Richards, D.M. Murphy, L. Lu, C.J. Kiely, D.J. Morgan, R.I. Smith, A.C. McLaughlin, D.E. Macphee, Improving the selectivity of photocatalytic NO x abatement through improved O2 reduction pathways using Ti0.909W0.091O2Nx semiconductor nanoparticles: from characterization to photocatalytic performance, ACS Catal. 8 (2018) 6927–6938, https://doi.org/10.1021/acscatal.8b00521.

[29] J. Patzsch, A. Folli, D.E. MacPhee, J.Z. Bloh, On the underlying mechanisms of the low observed nitrate selectivity in photocatalytic NOx abatement and the importance of the oxygen reduction reaction, Phys. Chem. Chem. Phys. 19 (2017) 32678–32686, https://doi.org/10.1039/c7cp05960d.

[30] O. Rosseler, M. Sleiman, V.N. Montesinos, A. Shavorskiy, V. Keller, N. Keller, M.I. Litter, H. Bluhm, M. Salmeron, H. Destaillats, Chemistry of NO x on TiO 2 surfaces studied by ambient pressure XPS: products, effect of UV irradiation, water, and coadsorbed K +, J. Phys. Chem. Lett. 4 (2013) 536–541, https://doi.org/10.1021/jz302119g.

[31] A.L. De Barros, A.A.Q. Domingos, P.B.A. Fechine, D. De Keukeleire, R.F. Do Nascimento, PET as a support material for TiO2 in advanced oxidation processes, J. Appl. Polym. Sci. 131 (2014) 1–9, https://doi.org/10.1002/app.40175.

[32] E. Pinter, F. Welle, E. Mayrhofer, A. Pechhacker, L. Motloch, V. Lahme, A. Grant, M. Tacker, Circularity study on pet bottle-to-bottle recycling, Sustainability 13 (2021), https://doi.org/10.3390/su13137370.

[33] M.J. Hernández Rodríguez, E. Pulido Melián, O. González Díaz, J. Araña, M. Macías, A. González Orive, J.M. Doña Rodríguez, Comparison of supported TiO2 catalysts in the photocatalytic degradation of NOx, J. Mol. Catal. Chem. 413 (2016) 56–66, https://doi.org/10.1016/j.molcata.2015.12.007.

[34] H. Adamu, A.J. McCue, R.S.F. Taylor, H.G. Manyar, J.A. Anderson, Influence of pretreatment on surface interaction between Cu and anatase-TiO2 in the simultaneous photoremediation of nitrate and oxalic acid, J. Environ. Chem. Eng. 7 (2019), https://doi.org/10.1016/j.jece.2019.103029.

[35] A.Y. Nosaka, T. Fujiwara, H. Yagi, H. Akutsu, Y. Nosaka, Characteristics of water adsorbed on TiO2 photocatalytic systems with increasing temperature as studied by solid-state1H NMR Spectroscopy, J. Phys. Chem. B 108 (2004) 9121–9125, https://doi.org/10.1021/jp037297i.

[36] Y. Hu, X. Song, S. Jiang, C. Wei, Enhanced photocatalytic activity of Pt-doped TiO2 for NOx oxidation both under UV and visible light irradiation: a synergistic effect of lattice Pt4+ and surface PtO, Chem. Eng. J. 274 (2015) 102–112, https://doi.org/10.1016/j.cej.2015.03.135.